

# Focal mechanisms of small earthquakes beneath the whole Japan Islands based on first-motion polarities picked using deep learning

Takahiko Uchide<sup>1,1</sup>

<sup>1</sup>National Institute of Advanced Industrial Science and Technology

November 30, 2022

## Abstract

Knowledge of crustal stress field is essential for understanding tectonics and earthquake generation. One way to estimate the crustal stress field is based on focal mechanisms of earthquakes. This study investigated focal mechanisms of ~ 110 thousand microearthquakes in Japan Islands shallower than 20 km based on the first-motion polarities picked by a simple neural network model, which was trained using two data sets: moderate to large earthquakes all over Japan and microearthquakes in two regions in Japan. The threshold of the confidence score from the neural network model was so chosen as to maximize the overall quality of focal mechanism solutions. The P- and T-axes of the numerous focal mechanism solutions provide more detailed distributions of crustal stress field. For example, in Chugoku region, there exist slight differences in the trend of P-axes azimuths between the northern and southern areas are observed, corresponding to the geodetic observations in space.

1 Focal mechanisms of small earthquakes beneath the whole  
2 Japan Islands based on first-motion polarities picked using  
3 deep learning

4 Takahiko Uchide<sup>1,\*</sup>

5 <sup>1</sup> Geological Survey of Japan, National Institute of Advanced Industrial Science and  
6 Technology (AIST)

7 \* Corresponding Author: Takahiko Uchide (t.uchide@aist.go.jp)

8 Key Points

- 9 ● Determined focal mechanisms of ~ 110,000 shallow inland earthquakes in Japan  
10 based on first-motion polarities by a neural network model.
- 11 ● Chose a threshold of the confidence score of the polarities to maximize the overall  
12 quality of focal mechanism solutions.
- 13 ● The numerous focal mechanism solutions indicate the crustal stress field at a fine  
14 scale.

15 Abstract

16 Knowledge of crustal stress field is essential for understanding tectonics and earthquake  
17 generation. One way to estimate the crustal stress field is based on focal mechanisms of

18 earthquakes. This study investigated focal mechanisms of ~ 110 thousand microearthquakes  
19 in Japan Islands shallower than 20 km based on the first-motion polarities picked by a  
20 simple neural network model, which was trained using two data sets: moderate to large  
21 earthquakes all over Japan and microearthquakes in two regions in Japan. The threshold of  
22 the confidence score from the neural network model was so chosen as to maximize the  
23 overall quality of focal mechanism solutions. The P- and T-axes of the numerous focal  
24 mechanism solutions provide more detailed distributions of crustal stress field. For example,  
25 in Chugoku region, there exist slight differences in the trend of P-axes azimuths between  
26 the northern and southern areas are observed, corresponding to the geodetic observations in  
27 space.

## 28 Plain Language Summary

29 The Earth's tectonic activities, such as creeping, mountain building, and earthquakes, are  
30 caused by internal forces (stress). Understanding the stress in the crust is important for  
31 understanding such tectonic activities and assessing future earthquakes. Conversely,  
32 earthquakes, especially ambient microearthquakes, can be a tool to investigate the crustal  
33 stress. We can estimate the focal mechanisms (fault geometry and slip direction of an  
34 earthquake) by considering the initial part of seismic waves goes up or down (first-motion  
35 polarities) at seismic stations. In this study, massive data from Japan were used. The  
36 polarities of ~ 2 million seismic data were measured using deep learning technique, and  
37 finally the focal mechanisms of ~ 110,000 earthquakes were determined. The result  
38 indicates the crustal stress distribution. Combination with other information such as the

39 ground surface deformation from geodesy, geography, and geology can enhance our  
40 understanding.

## 41 1. Introduction

42 Crustal stress field data are crucial to understand tectonics and seismic activity; however,  
43 measuring it at depths over a wide area is a challenge. Direct measurements at specific  
44 boreholes (e.g., Wu et al., 2007; Huffman et al., 2016; Brodsky et al., 2017; Townend et al.,  
45 2017) offer detailed information but only for one point. In contrast, seismology provides  
46 indirect measurements with more uncertainty but for a wide area. The focal mechanisms,  
47 which indicate the directions of fault plane and slip, indicate the orientation of the  
48 seismogenic stress. The World Stress Map (Heidbach et al., 2008; Heidbach et al., 2016;  
49 Heidbach et al., 2018) compiles this information all over the world.

50 In the past, routinely determined moment tensor solutions were used for estimating  
51 regional stress fields (Terakawa & Matsu'ura, 2010; Hardebeck, 2015). However, blank  
52 areas still exist even in seismically active area such as Japan Islands. More complete  
53 knowledge of the seismogenic stress field requires focal mechanisms of microearthquakes,  
54 especially in low seismicity areas (e.g., Imanishi et al., 2011; Imanishi et al., 2012;  
55 Matsumoto et al., 2015). Comprehensive investigations of microearthquake focal  
56 mechanisms reveal the regional stress field (e.g., Iio et al., 2018; Imanishi et al., 2019).

57 The focal mechanisms of moderate or larger earthquakes can be automatically  
58 determined using the full waveform from the local (e.g., Dreger & Helmberger, 1993;

59 Fukuyama et al., 1998) or global seismic network (e.g., Ekström et al., 2012). However, the  
60 mechanisms of small earthquakes cannot be similarly determined because of the difficulty  
61 of modeling high-frequency seismograms. We usually use the first-motion polarity: the  
62 vertical component initially goes either upward or downward. Automatic polarity-picking  
63 methods, such as one based on the sign of the first extremum after the P arrival (Nakamura,  
64 2004; Chen & Holland, 2016), have been developed. Pugh et al. (2016a) proposed a  
65 Bayesian approach using the first extremum and a probability function of P arrival time.  
66 Recently, deep learning has enabled us to automatically pick the polarity (Ross et al., 2018;  
67 Hara et al., 2019). Thus, we are technically ready to investigate large number of  
68 microearthquakes.

69 The aim of this study was to obtain the focal mechanism solutions in Japan Islands, one  
70 of the most seismically active regions in the world. The first-motion polarities were picked  
71 using a neural network model and seismic data from nationwide seismic networks. Finally,  
72 the focal mechanism solutions and spatial trends in P- and T-axes were studied.

## 73 2. Training the Neural Network Model

### 74 2.1. Data

75 The training of the neural network model was performed in two stages. In the first stage,  
76 the Hi-net data of 18,000 earthquakes with P arrival and polarity data in the JMA catalog  
77 were used. Most of these earthquakes are larger than  $M$  3 (Figure S1). The whole data were  
78 then spatially divides into the training and validation data sets (Figure 1a, Table 1).

79 In the second stage, I used the P arrival time and polarity of microearthquakes in Kanto  
80 and Chugoku regions, manually picked by Geological Survey of Japan, National Institute  
81 of Advanced Industrial Science and Technology (AIST). The Kanto data were used by  
82 Imanishi et al. (2019). The spatial distributions of used events in Kanto and Chugoku  
83 regions are shown in Figures 1b and 1c, respectively. The number of seismogram sets and  
84 earthquakes is summarized in Table 1.

85 In the both stages, seismograms of three components (up-down, north-south, and  
86 east-west) were used. Each component had 256 samples: 156 samples before and 100  
87 samples after P arrival. The samples are 2.56-s long, as the data were sampled at 100 Hz.  
88 Low-frequency noise was removed by applying a high-pass filter at 1 Hz. I emphasized the  
89 initial portion of the P-wave by clipping seismograms at a certain threshold.

90 Furthermore, I augmented the data four times by flipping all three components, rotating  
91 horizontal components by randomly selected angles, and time-shifting. The flipping  
92 procedure equalizes the number of positive and negative polarity data. The time shift  
93 addresses potential misalignment of data due to uncertainties in the arrival time picking.

94 Later, I examined various values of the clipping threshold and the time-shift range.

## 95 2.2. Design of the Neural Network Model

96 Figure 2 summarizes the neural network used in this study. The input of the neural  
97 network models is a three-component 256-sample long seismogram set where the 156th  
98 sample corresponds to the P-arrival time already picked either manually or automatically.

99 The output comprises two scores corresponding to the upward and downward polarities.  
100 Note that, in the case of Southern California, Ross et al. (2018) classified the polarity as  
101 “Up,” “Down,” and “Unknown”; however, in this study, the “Unknown” class is not set.  
102 The data set contained many seismograms with impulsive onset but no polarity information  
103 (e.g., Figure S2), and the lack of polarity information does not mean “Unknown” in this  
104 case.

105 I designed a simple neural network model (Figure 2) similar to the ones used in prior  
106 studies (Ross et al., 2018; Hara et al., 2019). The neural network model started with two  
107 convolution layers, followed by three units composed of convolution, batch-normalization  
108 (Ioffe & Szegedy, 2015), and pooling layers. The models ended with two fully connected  
109 layers. The kernel size of the convolutional layers was 11. For all but the final layers,  
110 the activation function was the Rectified Linear Units (ReLU) (Nair & Hinton, 2010);  
111 SoftMax function was chosen for the final layer:

$$\text{softmax}(\mathbf{z})_i = \frac{\exp(z_i)}{\sum_j \exp(z_j)}, \#(1)$$

112 where  $\mathbf{z} = (z_1, z_2)$  is the output of the final layer corresponding to the positive and negative  
113 polarities, respectively. Then, the outputs are non-negative, and their summation is always 1.  
114 In order to address the overfitting problem, the dropout technique (Srivastava et al., 2014)  
115 was adopted: 50 % of randomly selected perceptions were muted during the training. The  
116 loss was evaluated by the negative log-likelihood function and the parameters of the neural  
117 network model were updated by back-propagating the loss (Rumelhart et al., 1986)  
118 optimized by the adaptive moment estimation (Adam) method (Kingma & Ba, 2014).

119 2.3. Result

120 Hundred cases with randomly selected clipping thresholds in the range of  $10^{-6}$  to  $10^{-4}$   
121 m/s and the half-width of the time-shift ranging 0–30 samples were examined. The result  
122 was evaluated based on the loss value for the test data set. The result shows that the shorter  
123 half-width of the time-shift range, the smaller is the loss (Figure 3a). The clipping threshold  
124 has no correlation with the loss value (Figure 3b).

125 Hereafter, I did not apply time-shift and used  $10^{-5}$  m/s as the clipping threshold. The  
126 neural network model was trained using these values. The precision-recall curve of the  
127 trained model is shown in Figure 3c.

128 3. Application to Crustal Earthquakes in Japan

129 I applied the trained model to event data of earthquakes that occurred in the period 2005–  
130 2019 at depths less than 20 km within the coastline, excluding the events for which polarity  
131 information is already available in the catalog (Table 1). I used seismograms from Hi-net  
132 and the JMA seismic network with P-wave arrival times in the JMA catalog. Preprocessing  
133 was done in the same way as the training. Good results were obtained for polarity picking  
134 with high scores (Figure 4), even in noisy cases.

135 The focal mechanisms were determined using polarity information with scores larger  
136 than a confidence threshold and the HASH code (Hardebeck & Shearer, 2002, 2008). The  
137 quality of focal mechanisms depends on the confidence threshold (Figure 3d). If the  
138 threshold is too high, the very small number of polarity picks cannot constrain focal

139 mechanisms well. If the threshold is lower than 0.7, the fraction of A and B ranks given by  
140 the HASH code (Hardebeck & Shearer, 2008) is almost constant. I adopted a confidence  
141 threshold of 0.7.

142 Figure 5 shows the estimated focal mechanisms and their P- and T- axes in addition to  
143 the NIED F-net Moment Tensor solutions for reference. The focal mechanisms of 113,700  
144 events are estimated, while those of 6830 events are undetermined because the number of  
145 stations was smaller than 8. Ranks A, B, C, and D by the HASH code (Hardebeck &  
146 Shearer, 2008) were given to 1060, 17890, 36958, and 50962 events, respectively. The  
147 focal mechanism solutions cover much more space than those in a routine catalog.

148 The obtained P- and T-axes (Figures 5c and 5d, respectively) are well consistent with  
149 stress regimes reported in prior studies: north-south extensional stress field in Kyushu  
150 region (Matsumoto et al., 2015; Savage et al., 2016); normal faulting earthquakes in the  
151 area of Fukushima-Hamadori and northern Ibaraki prefecture (Imanishi et al., 2012).

## 152 4. Discussion

153 It may be surprising that the narrower time-shift range of the data, the better is the model  
154 performance, because the time-shifting would make the model more flexible and robust to  
155 uncertainties in arrival time picking. There are two potential reasons. One is that the arrival  
156 times in the test data were accurate because of careful review by an analyst, and therefore  
157 the time-shift was not really required. Another possible reason is the shortage of training  
158 data from microearthquakes.

159 Determination of focal mechanisms from the first-motion polarities of P-waves picked  
160 by the trained neural network model is also important for assessing the quality of polarity  
161 picking. In this study 50.8 % of the focal mechanism solutions are ranked D or  
162 undetermined. In a study on the determination of the focal mechanisms of earthquakes in  
163 Southern California using manually picked P-wave polarity and the amplitude ratio of P  
164 and S waves (Yang et al., 2012), the results showed that 56.6 % (101,309 out of 178,899  
165 events) of the events were ranked D, comparable to the result of this study. Thus, this study  
166 yields a reasonable quality of the P-wave first-motion polarity picking, though the  
167 comparison is not simple because of many factors including the differences in the  
168 observational conditions such as the magnitude range and station density. Focal mechanism  
169 determination can be improved in several ways: introduction of P-wave amplitude (e.g.,  
170 Matsushita & Imanishi, 2015; Pugh et al., 2016b) and the ratio of P- and S-wave  
171 amplitudes (Hardebeck & Shearer, 2003; Yang et al., 2012), as well as the advances in the  
172 P-wave polarity picking.

173 The quality of the focal mechanism solutions is shown by region in Figure 3e. In  
174 particular, the quality in Hokkaido region is much worse than in other regions. The reason  
175 was examined by focusing on the number of stations. First, the quality of the focal  
176 mechanism solutions is well correlated with the number of stations (Figure 3f). Next, the  
177 number of usable stations is smaller in Hokkaido than in other regions. This is probably  
178 because of the spatial density of seismic stations (Figure 5e). Hence, it is more difficult to  
179 determine the focal mechanisms in Hokkaido than elsewhere.

180 We see interesting features in the spatial distribution of the P- and T-axis azimuths  
181 (Figures 5c and 5d). For example, in Chugoku region, the P-axes strike in the east–west  
182 direction in the northern area (San-in area), whereas those strike in the NW–SE direction in  
183 the southern one (Sanyo area). The contrast in the P-axis azimuths in western Tottori was  
184 reported by Kawanishi et al. (2009). This study too shows a similar trend over the whole  
185 Chugoku region. This contrast geographically corresponds to the San-in shear zone  
186 (Meneses-Gutierrez & Nishimura, 2020). A combination of this study with geodetic  
187 implications will enhance our understanding of seismotectonics.

188 In spite of the dramatic increase in focal mechanism solutions, there are still blank areas  
189 in Japan Islands. The seismicity is quite low in such areas. Hence, this kind of study may  
190 need to be performed even for smaller earthquakes, which is a greater challenge than that  
191 tackled in the present study. Additional campaign seismic observations may improve the  
192 focal mechanism solutions of very small earthquakes. In addition, combining these  
193 observations with various observations including geological, geographical, and geodetical  
194 ones will improve our understanding of the crustal stress field and its origin.

## 195 5. Conclusions

196 In this study, the focal mechanisms of small to microearthquakes are estimated for better  
197 understanding of the crustal stress fields in Japan Islands. The focal mechanisms were  
198 derived using the P-wave first-motion polarities picked by a neural network model that  
199 takes three-component seismograms with P arrival times as the input. The focal  
200 mechanisms of almost all microearthquakes over the whole of Japan Islands were

201 successfully determined. The focal mechanism solutions are generally consistent with the  
202 stress regime on a large scale. The slight but clear differences in the P-axis azimuths in the  
203 northern and southern parts of Chugoku region are consistent with the geodetic  
204 observations for this region. The results of this study will be useful for revealing the crustal  
205 stress field, and thus, for assessing the past and current tectonic activities and future  
206 earthquake generation.

## 207 Acknowledgements

208 I thank Kazutoshi Imanishi and Reiken Matsushita for providing phase data for  
209 microearthquakes in Kanto and Chugoku regions in Japan. I also thank the NIED,  
210 especially Takanori Matsuzawa, for helping me prepare the large seismic data set. I used  
211 seismic data from NIED Hi-net (National Research Institute for Earth Science and Disaster  
212 Resilience, 2020) and JMA available at <http://www.hinet.bosai.go.jp/?LANG=en> (last  
213 accessed on 25 March 2020), the phase data from JMA Unified Earthquake Catalog,  
214 available at [http://www.data.jma.go.jp/svd/eqev/data/bulletin/eqdoc\\_e.html](http://www.data.jma.go.jp/svd/eqev/data/bulletin/eqdoc_e.html) (last accessed  
215 on 25 March 2020) and <http://www.hinet.bosai.go.jp/?LANG=en> (last accessed on 25  
216 March 2020), and the moment tensor solutions by NIED F-net project (Fukuyama et al.,  
217 1998) available at <http://www.fnet.bosai.go.jp/top.php?LANG=en> (last accessed on 25  
218 March 2020). The data analyses in this study were performed using PyTorch (Paszke et al.,  
219 2019), ObsPy (Beyreuther et al., 2010; Megies et al., 2011; Krischer et al., 2015), HASH  
220 (Hardebeck & Shearer, 2002, 2008), and HASHpy (Williams, 2014). I used Generic  
221 Mapping Tools (Wessel et al., 2013) for generating Figures 1, 3, 5, and S1, and Matplotlib

222 (Hunter, 2007) for Figures 4 and S2. This work was supported by Mitsubishi Foundation  
223 and AIST EDGE Runners project. In this work, the computation facility of the AI Bridging  
224 Cloud Infrastructure (ABCI) maintained by AIST was employed.

## 225 References

- 226 Amante, C., & Eakins, B. W. (2009). *ETOPO1 1 Arc-Minute Global Relief Model:  
227 Procedures, Data Sources and Analysis*. NOAA Technical Memorandum NESDIS  
228 NGDC-24. National Geophysical Data Center, NOAA.  
229 <https://doi.org/10.7289/V5C8276M>
- 230 Beyreuther, M., Barsch, R., Krischer, L., Megies, T., Behr, Y., & Wassermann, J. (2010).  
231 ObsPy: A Python Toolbox for Seismology. *Seismological Research Letters*, 81(3),  
232 530-533. <https://doi.org/10.1785/gssrl.81.3.530>
- 233 Brodsky, E. E., Saffer, D., Fulton, P., Chester, F., Conin, M., Huffman, K., et al. (2017). The  
234 postearthquake stress state on the Tohoku megathrust as constrained by reanalysis of  
235 the JFAST breakout data. *Geophysical Research Letters*, 44(16), 8294-8302.  
236 <https://doi.org/10.1002/2017gl074027>
- 237 Chen, C., & Holland, A. A. (2016). PhasePAPy: A Robust Pure Python Package for  
238 Automatic Identification of Seismic Phases. *Seismological Research Letters*, 87(6),  
239 1384-1396. <https://doi.org/10.1785/0220160019>
- 240 Dreger, D. S., & Helmberger, D. V. (1993). Determination of source parameters at regional  
241 distances with three-component sparse network data. *Journal of Geophysical  
242 Research*, 98(B5), 8107-8125. <https://doi.org/10.1029/93JB00023>

- 243 Ekström, G., Nettles, M., & Dziewoński, A. M. (2012). The global CMT project 2004–  
244 2010: Centroid-moment tensors for 13,017 earthquakes. *Physics of the Earth and*  
245 *Planetary Interiors*, 200–201, 1-9. <https://doi.org/10.1016/j.pepi.2012.04.002>
- 246 Fukuyama, E., Ishida, M., Dreger, D. S., & Kawai, H. (1998). Automated seismic moment  
247 tensor determination by using on-line broadband seismic waveforms. *Zisin 2nd*  
248 *Series*, 51(1), 149-156. [https://doi.org/10.4294/zisin1948.51.1\\_149](https://doi.org/10.4294/zisin1948.51.1_149) (in Japanese  
249 with English abstract)
- 250 Hara, S., Fukahata, Y., & Iio, Y. (2019). P-wave first-motion polarity determination of  
251 waveform data in western Japan using deep learning. *Earth, Planets and Space*,  
252 71(1), 127. <https://doi.org/10.1186/s40623-019-1111-x>
- 253 Hardebeck, J. L. (2015). Stress orientations in subduction zones and the strength of  
254 subduction megathrust faults. *Science*, 349(6253), 1213-1216.  
255 <https://doi.org/10.1126/science.aac5625>
- 256 Hardebeck, J. L., & Shearer, P. M. (2002). A new method for determining first-motion focal  
257 mechanisms. *Bulletin of the Seismological Society of America*, 92(6), 2264-2276.
- 258 Hardebeck, J. L., & Shearer, P. M. (2003). Using S/P amplitude ratios to constrain the focal  
259 mechanisms of small earthquakes. *Bulletin of the Seismological Society of America*,  
260 93(6), 2434-2444.
- 261 Hardebeck, J. L., & Shearer, P. M. (2008). HASH: A FORTRAN program for computing  
262 earthquake first-motion focal mechanisms – v1.2 –. Retrieved from  
263 <http://earthquake.usgs.gov/research/software/HASH/hash.v1.2.tar.gz>
- 264 Heidbach, O., Rajabi, M., Cui, X., Fuchs, K., Müller, B., Reinecker, J., et al. (2018). The

- 265 World Stress Map database release 2016: Crustal stress pattern across scales.  
266 *Tectonophysics*, 744, 484-498.  
267 <https://doi.org/https://doi.org/10.1016/j.tecto.2018.07.007>
- 268 Heidbach, O., Rajabi, M., Reiter, K., Ziegler, M., & Team, W. (2016). *World Stress Map*  
269 *Database Release 2016*. GFZ Data Services.  
270 <https://doi.org/10.5880/WSM.2016.001>
- 271 Heidbach, O., Tingay, M., Barth, A., Reinecker, J., Kurfeß, D., & Müller, B. (2008). *The*  
272 *World Stress Map database release 2008*.  
273 <https://doi.org/10.1594/GFZ.WSM.Rel2008>
- 274 Huffman, K. A., Saffer, D. M., & Dugan, B. (2016). In situ stress magnitude and rock  
275 strength in the Nankai accretionary complex: a novel approach using paired  
276 constraints from downhole data in two wells. *Earth, Planets and Space*, 68(1), 123.  
277 <https://doi.org/10.1186/s40623-016-0491-4>
- 278 Hunter, J. D. (2007). Matplotlib: A 2D Graphics Environment. *Computing in Science &*  
279 *Engineering*, 9(3), 90-95. <https://doi.org/10.1109/MCSE.2007.55>
- 280 Iio, Y., Kishimoto, S., Nakao, S., Miura, T., Yoneda, I., Sawada, M., & Katao, H. (2018).  
281 Extremely weak fault planes: An estimate of focal mechanisms from stationary  
282 seismic activity in the San'in district, Japan. *Tectonophysics*, 723, 136-148.  
283 <https://doi.org/10.1016/j.tecto.2017.12.007>
- 284 Imanishi, K., Ando, R., & Kuwahara, Y. (2012). Unusual shallow normal-faulting  
285 earthquake sequence in compressional northeast Japan activated after the 2011 off  
286 the Pacific coast of Tohoku earthquake. *Geophysical Research Letters*, 39(9),

- 287 L09306. <https://doi.org/10.1029/2012GL051491>
- 288 Imanishi, K., Kuwahara, Y., Takeda, T., Mizuno, T., Ito, H., Ito, K., et al. (2011).  
289 Depth-dependent stress field in and around the Atotsugawa fault, central Japan,  
290 deduced from microearthquake focal mechanisms: Evidence for localized aseismic  
291 deformation in the downward extension of the fault. *Journal of Geophysical*  
292 *Research*, 116(B1), B01305. <https://doi.org/10.1029/2010JB007900>
- 293 Imanishi, K., Uchide, T., Ohtani, M., Matsushita, R., & Nakai, M. (2019). Construction of  
294 the crustal stress map in the Kanto region, central Japan. *Bulletin of the Geological*  
295 *Survey of Japan*, 70(3), 273-298. (in Japanese with English abstract)
- 296 Ioffe, S., & Szegedy, C. (2015). Batch normalization: accelerating deep network training by  
297 reducing internal covariate shift. *ArXiv e-prints*. Retrieved from  
298 <https://ui.adsabs.harvard.edu/#abs/2015arXiv150203167I>
- 299 Kawanishi, R., Iio, Y., Yukutake, Y., Shibutani, T., & Katao, H. (2009). Local stress  
300 concentration in the seismic belt along the Japan Sea coast inferred from precise  
301 focal mechanisms: Implications for the stress accumulation process on intraplate  
302 earthquake faults. *Journal of Geophysical Research Solid Earth*, 114(B1).  
303 <https://doi.org/10.1029/2008jb005765>
- 304 Kingma, D. P., & Ba, J. (2014). Adam: A method for stochastic optimization. *arXiv preprint*  
305 *arXiv:1412.6980*.
- 306 Krischer, L., Megies, T., Barsch, R., Beyreuther, M., Lecocq, T., Caudron, C., &  
307 Wassermann, J. (2015). ObsPy: a bridge for seismology into the scientific Python  
308 ecosystem. *Computational Science & Discovery*, 8(1).

- 309 <https://doi.org/10.1088/1749-4699/8/1/014003>
- 310 Matsumoto, S., Nakao, S., Ohkura, T., Miyazaki, M., Shimizu, H., Abe, Y., et al. (2015).  
311 Spatial heterogeneities in tectonic stress in Kyushu, Japan and their relation to a  
312 major shear zone. *Earth, Planets and Space*, 67(1), 172.  
313 <https://doi.org/10.1186/s40623-015-0342-8>
- 314 Matsushita, R., & Imanishi, K. (2015). Stress fields in and around metropolitan Osaka,  
315 Japan, deduced from microearthquake focal mechanisms. *Tectonophysics*, 642,  
316 46-57. <https://doi.org/10.1016/j.tecto.2014.12.011>
- 317 Megies, T., Beyreuther, M., Barsch, R., Krischer, L., & Wassermann, J. (2011). ObsPy –  
318 What can it do for data centers and observatories? *Annals of Geophysics*, 54(1), 12.  
319 <https://doi.org/10.4401/ag-4838>
- 320 Meneses-Gutierrez, A., & Nishimura, T. (2020). Inelastic deformation zone in the lower  
321 crust for the San-in Shear Zone, Southwest Japan, as observed by a dense GNSS  
322 network. *Earth, Planets and Space*, 72(1), 10.  
323 <https://doi.org/10.1186/s40623-020-1138-z>
- 324 Nair, V., & Hinton, G. E. (2010). *Rectified linear units improve restricted boltzmann*  
325 *machines*. Paper presented at the 27th International Conference on Machine  
326 Learning (ICML-10), Haifa, Israel, 807-814.
- 327 Nakamura, M. (2004). Automatic determination of focal mechanism solutions using initial  
328 motion polarities of P and S waves. *Physics of the Earth and Planetary Interiors*,  
329 146(3), 531-549. <https://doi.org/10.1016/j.pepi.2004.05.009>
- 330 National Research Institute for Earth Science and Disaster Resilience. (2020). *NIED Hi-net*.

- 331 <https://doi.org/10.17598/NIED.0003>
- 332 Paszke, A., Gross, S., Massa, F., Lerer, A., Bradbury, J., Chanan, G., et al. (2019). PyTorch:  
333 An imperative style, high-performance deep learning library. In *Advances in Neural*  
334 *Information Processing Systems* (Vol. 32, pp. 8024-8035) Curran Associates, Inc.
- 335 Pugh, D. J., White, R. S., & Christie, P. A. F. (2016a). Automatic Bayesian polarity  
336 determination. *Geophysical Journal International*, 206(1), 275-291.  
337 <https://doi.org/10.1093/gji/ggw146>
- 338 Pugh, D. J., White, R. S., & Christie, P. A. F. (2016b). A Bayesian method for microseismic  
339 source inversion. *Geophysical Journal International*.  
340 <https://doi.org/10.1093/gji/ggw186>
- 341 Ross, Z. E., Meier, M.-A., & Hauksson, E. (2018). P wave arrival picking and first-motion  
342 polarity determination with deep learning. *Journal of Geophysical Research Solid*  
343 *Earth*, 123(6), 5120-5129. <https://doi.org/10.1029/2017JB015251>
- 344 Rumelhart, D. E., Hinton, G. E., & Williams, R. J. (1986). Learning representations by  
345 back-propagating errors. *Nature*, 323(6088), 533-536.  
346 <https://doi.org/10.1038/323533a0>
- 347 Savage, M. K., Aoki, Y., Unglert, K., Ohkura, T., Umakoshi, K., Shimizu, H., et al. (2016).  
348 Stress, strain rate and anisotropy in Kyushu, Japan. *Earth and Planetary Science*  
349 *Letters*, 439, 129-142. <https://doi.org/10.1016/j.epsl.2016.01.005>
- 350 Shearer, P. M., Prieto, G. A., & Hauksson, E. (2006). Comprehensive analysis of  
351 earthquake source spectra in Southern California. *Journal of Geophysical Research*,  
352 *III*(B6), B06303. <https://doi.org/10.1029/2005JB003979>

- 353 Srivastava, N., Hinton, G., Krizhevsky, A., Sutskever, I., & Salakhutdinov, R. (2014).  
354 Dropout: a simple way to prevent neural networks from overfitting. *The Journal of*  
355 *Machine Learning Research*, 15(1), 1929-1958.
- 356 Terakawa, T., & Matsu'ura, M. (2010). The 3-D tectonic stress fields in and around Japan  
357 inverted from centroid moment tensor data of seismic events. *Tectonics*, 29(6),  
358 TC6008. <https://doi.org/10.1029/2009TC002626>
- 359 Townend, J., Sutherland, R., Toy, V. G., Doan, M.-L., C  lerier, B., Massiot, C., et al. (2017).  
360 Petrophysical, Geochemical, and Hydrological Evidence for Extensive  
361 Fracture-Mediated Fluid and Heat Transport in the Alpine Fault's Hanging-Wall  
362 Damage Zone. *Geochemistry, Geophysics, Geosystems*, 18(12), 4709-4732.  
363 <https://doi.org/10.1002/2017GC007202>
- 364 Wessel, P., Smith, W. H. F., Scharroo, R., Luis, J., & Wobbe, F. (2013). Generic Mapping  
365 Tools: Improved Version Released. *Eos, Transactions American Geophysical Union*,  
366 94(45), 409-410. <https://doi.org/10.1002/2013eo450001>
- 367 Williams, M. C. (2014). HASHpy. Retrieved from <https://doi.org/10.5281/zenodo.9808>
- 368 Wu, H.-Y., Ma, K.-F., Zoback, M., Boness, N., Ito, H., Hung, J.-H., & Hickman, S. (2007).  
369 Stress orientations of Taiwan Chelungpu-Fault Drilling Project (TCDP) hole-A as  
370 observed from geophysical logs. *Geophysical Research Letters*, 34(1).  
371 <https://doi.org/10.1029/2006gl028050>
- 372 Yang, W., Hauksson, E., & Shearer, P. M. (2012). Computing a large refined catalog of  
373 focal mechanisms for southern California (1981–2010): Temporal stability of the  
374 style of faulting. *Bulletin of the Seismological Society of America*, 102(3),

375 1179-1194. <https://doi.org/10.1785/0120110311>

376

377

378 Tables

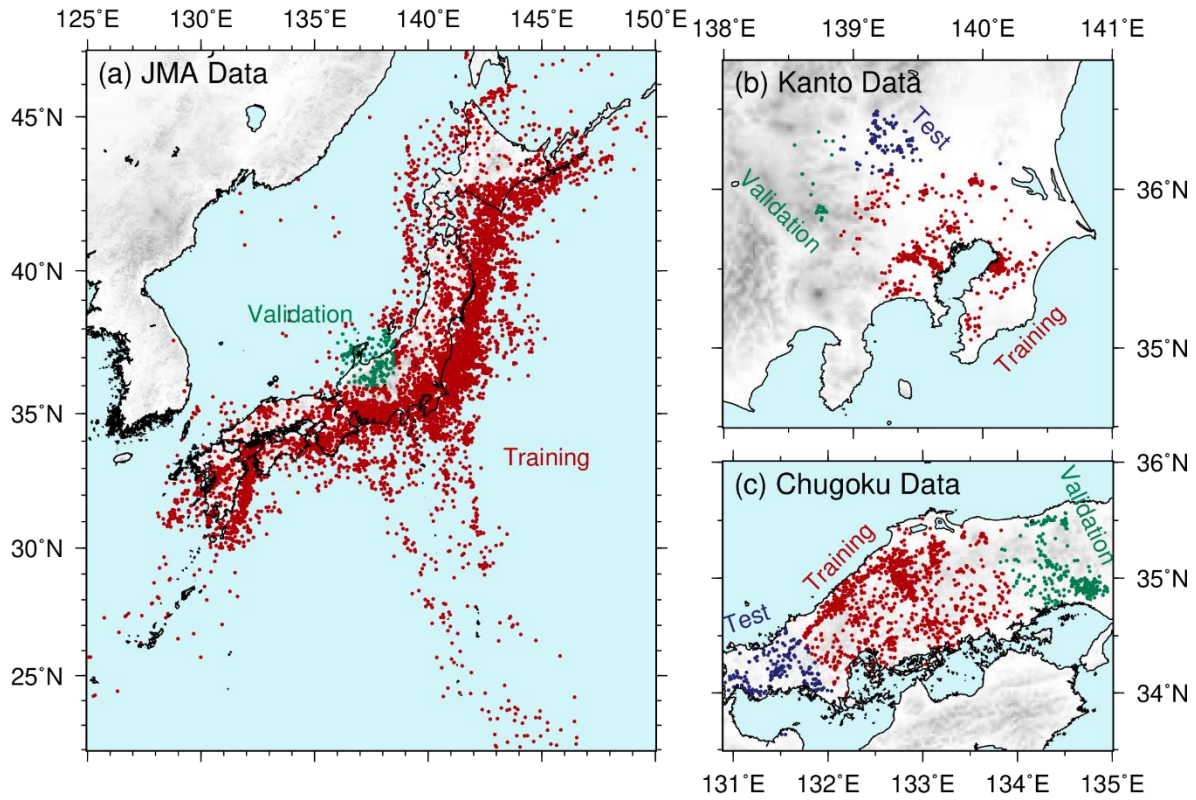
379 Table 1

380 Numbers of seismograms and earthquakes contained in data sets.

Region	Type of Data Set	Seismogram Sets	Earthquakes
All Japan	Training	279,483	17,402
	Validation	7,666	598
Kanto	Training	12,814	1,262
	Validation	784	56
	Test	1,483	113
Chugoku	Training	63,359	2,259
	Validation	7,674	322
	Test	12,838	595
All Japan	Application	1,930,132	113,700

381

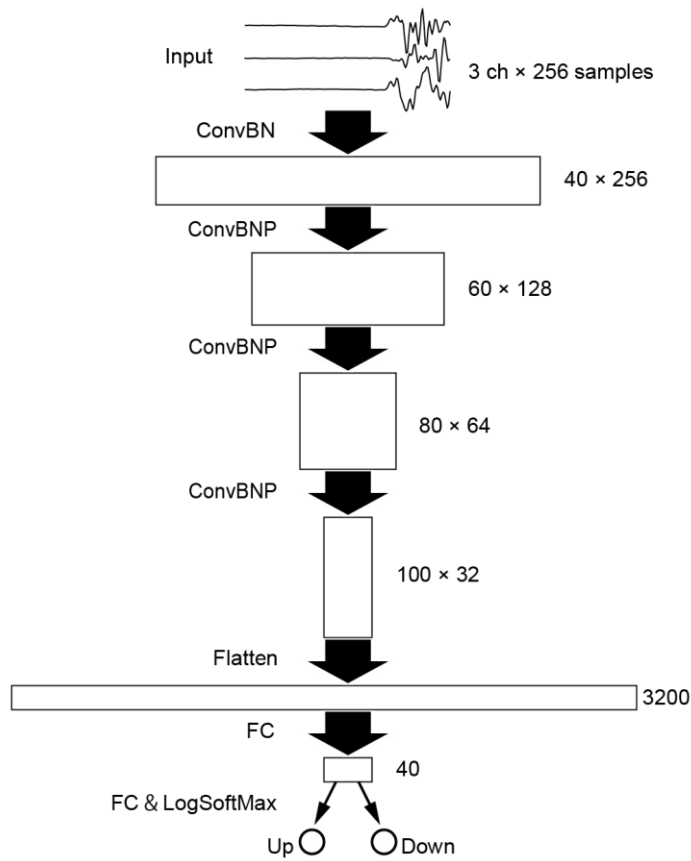
382 Figures



383

384 Figure 1

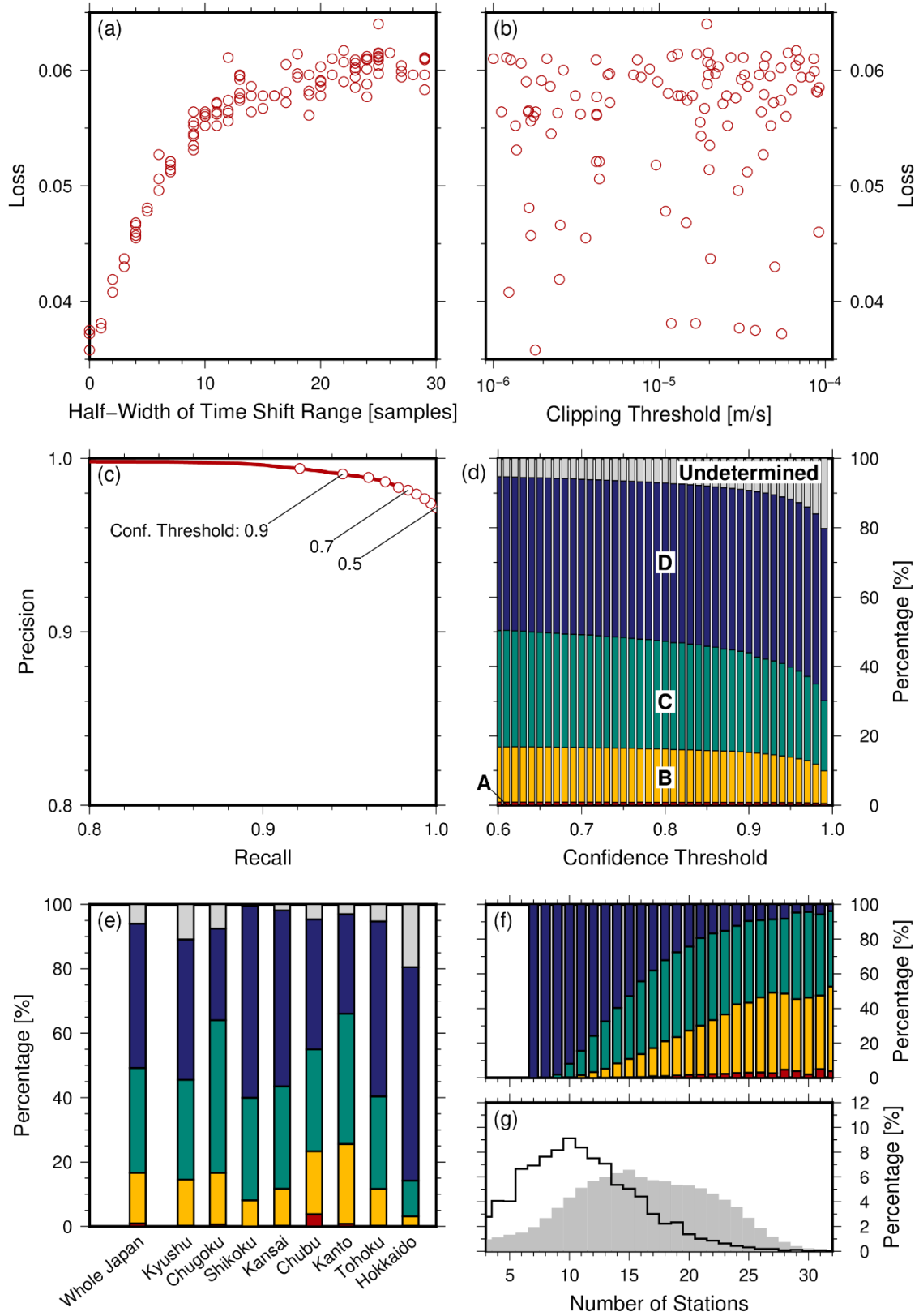
385 Distribution of the epicenters of the earthquakes used for training (red), validation  
386 (green), and testing (blue) of the neural network model. Topography is from ETOPO1  
387 (Amante & Eakins, 2009).



388

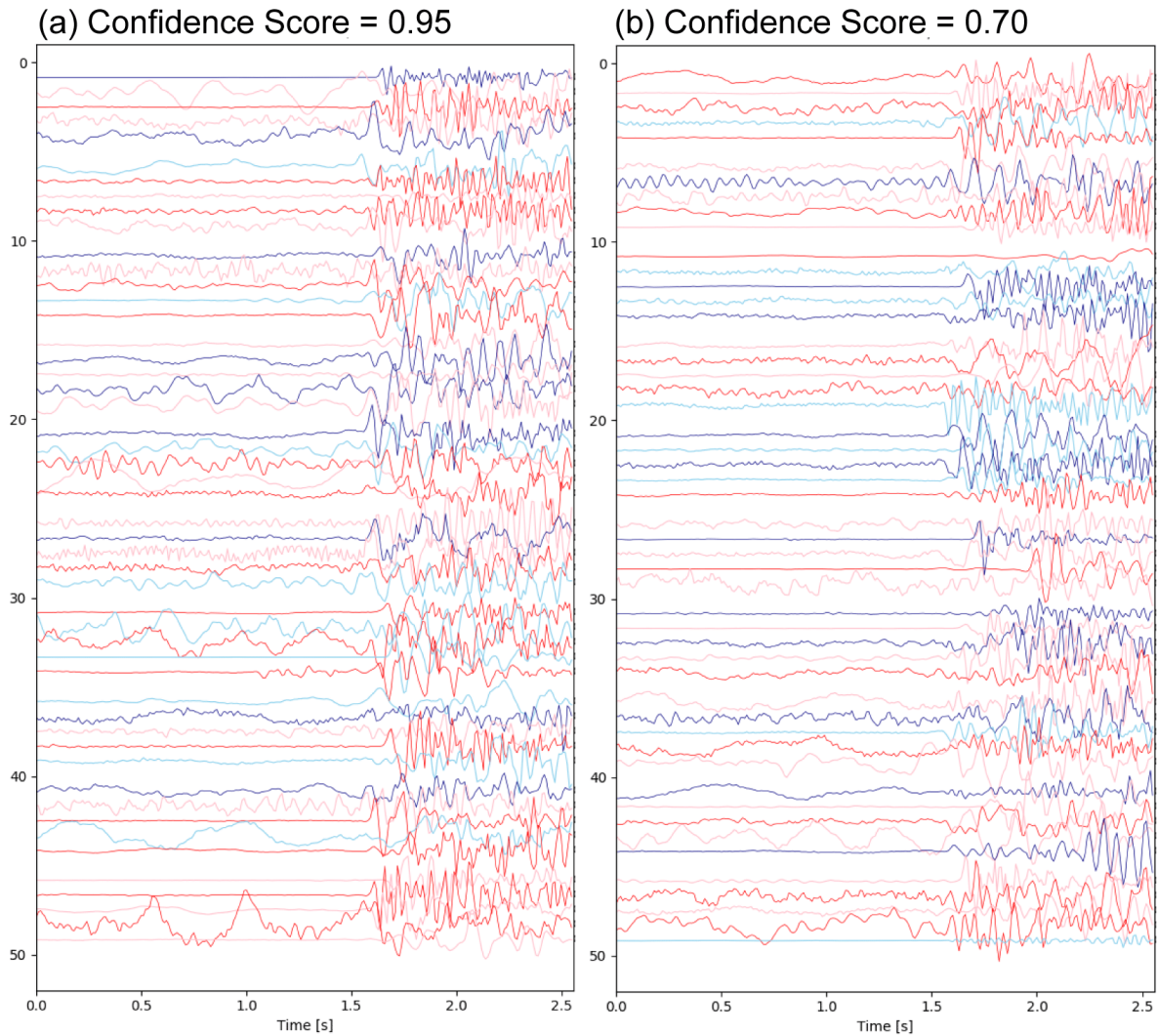
389 Figure 2

390 Design of the neural network model. Numbers on the right indicate the number of  
391 channels and samples. “ConvBN,” “Conv BNP,” and “FC” denote convolution and batch  
392 normalization layers; convolution, batch normalization, and pooling layers; and fully  
393 connected layers, respectively.



395 **Figure 3**

396 Summary of the results. Here, (a) and (b) show the loss function values as functions of  
397 the time-shift range and the clipping threshold, respectively. (c) Precision-recall curve of  
398 the trained model for the test data set. Circles correspond to every 0.05 units of the  
399 confidence thresholds. (d) Bar graphs of the rank of focal mechanism solutions as a  
400 function of the confidence threshold. (e) Bar graphs of the rank of focal mechanism  
401 solutions for the whole of Japan and eight regions. Here a model with a confidence  
402 threshold of 0.7 was used. (f) Bar graphs as a function of the number of stations. (g)  
403 Histograms of events as a function of the number of stations. The black line and gray  
404 shaded region indicate the values for Hokkaido and other regions, respectively.



405

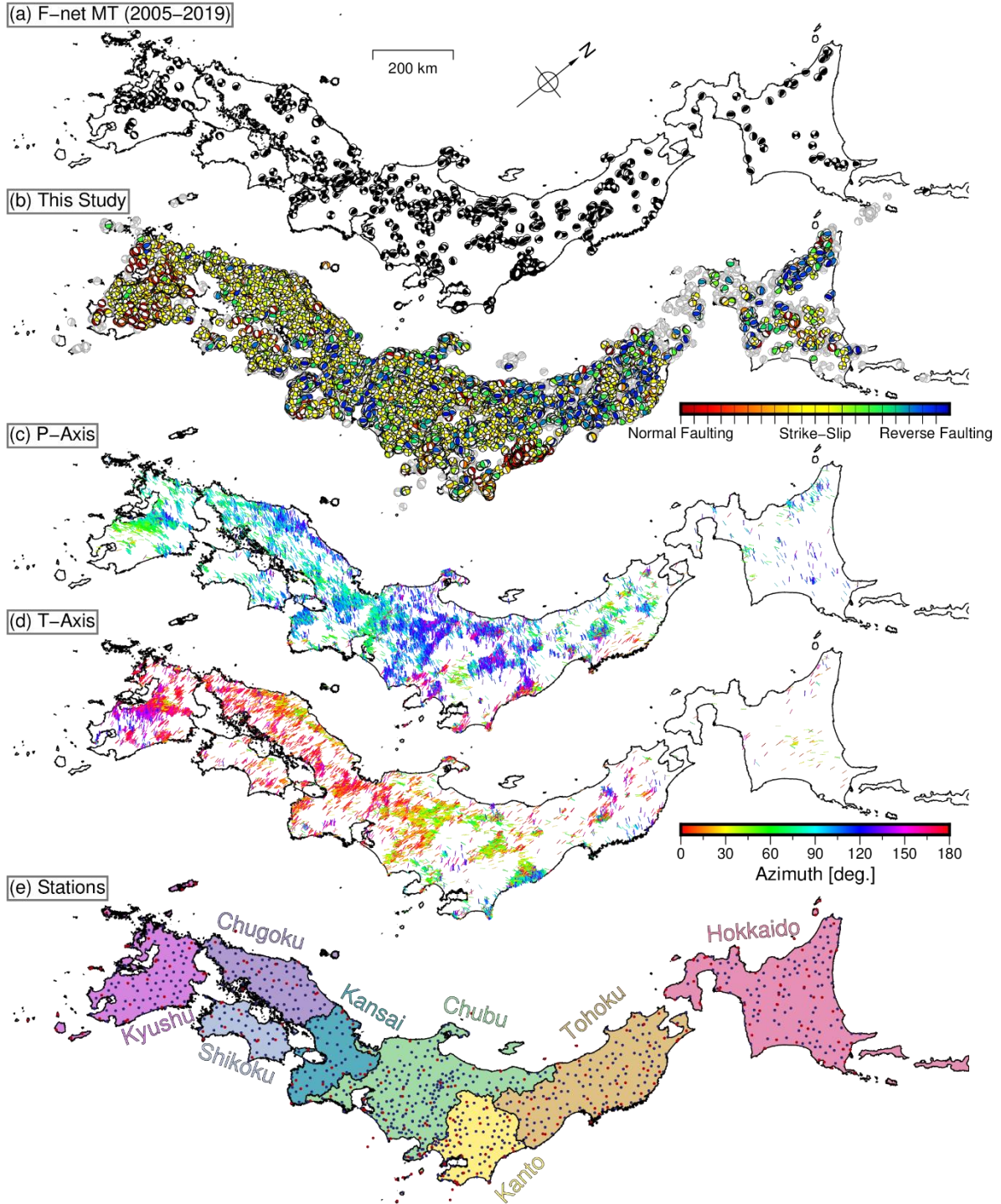
406 **Figure 4**

407 Examples of polarities picked by the neural network model with confidence scores of (a)

408 0.95 and (b) 0.70. Seismograms with negative polarities are flipped. If correctly picked, the

409 first motion looks positive in this figure. Light and dark colors are alternatively for

410 convenience.



411

412 Figure 5

413 (a) Moment tensor solutions of earthquakes in 2006-2019 by NIED F-net Project

414 (Fukuyama et al., 1998), for reference. (b) Focal mechanism solutions in this study.  
415 Solutions ranked A–C (Hardebeck & Shearer, 2008) are colored according to focal  
416 mechanism types (Shearer et al., 2006). Solution ranked D are shown by gray beach balls.  
417 (c) Azimuths of the P-axes of the estimated focal mechanism solutions ranked A – C and  
418 with less than 30° of plunge. Colors indicate the azimuths. (d) Azimuths of the T-axes. (e)  
419 Station distribution.